EES Solar

ROYAL SOCIETY OF CHEMISTRY

PAPER

View Article Online
View Journal | View Issue

Check for updates

Cite this: *EES Sol.*, 2025, **1**, 857

Oxygen-inducing effects in metal halide perovskite thin films for solar cells

Selengesuren Suragtkhuu,[a] Purevlkham Myagmarsereejid,[a] Quang Thang Trinh,[a] Tuul Tsagaantsooj,[b] Ashley D. Slattery,[c] Abraham Adenle,[a] Solongo Purevdorj,[a] Eric Campbell,[a] Oisín E. FitzGerald,[d] Taylor J. Z. Stock,[de] Sina Jamali,[a] Thomas J. Macdonald,[d] Tim Gould,[a] Nam-Trung Nguyen,[a] Chihaya Adachi,[b] Yu Lin Zhong[a] and Munkhbayar Batmunkh*[a]

Received 21st June 2025
Accepted 20th August 2025

DOI: 10.1039/d5el00098j

rsc.li/EESSolar

Perovskite solar cells (PSCs) have attracted increasing attention with their high efficiency and low cost. However, their journey towards commercialization is currently hindered by the issues associated with degradations in the ambient environment and under other harsh conditions. These stability-related issues can be associated with several reasons such as halide vacancies, structural defects, ion migrations and others within the perovskite structures. Herein, we studied the effect of an oxygen-inducing strategy on metal halide perovskites to reduce their halide vacancies for stable solar cells. It was found that perovskite films with the precisely controlled oxygen amount show improved photovoltaic performances, including fill factor and open-circuit voltage, when utilized in solar cells. We showed that the presence of oxygen plays a crucial role in increasing the efficiency and stability of solar cells due to the improvements in the structural uniformity and grain size, and thus suppresses charge and nonradiative recombination. More importantly, the oxygen-induced α-FAPbI$_3$-based PSCs retained nearly 50% of their initial efficiencies while the devices without oxygen maintained less than 10% of their initial values after harsh testing conditions, demonstrating excellent structural stability and water tolerance.

Broader context

The rapid development of perovskite solar cells has sparked global interest in next-generation photovoltaics due to their remarkable power conversion efficiencies and low manufacturing costs. Despite their promise, these photovoltaic systems face significant challenges in long-term operational stability under ambient conditions such as humidity. These degradation pathways, largely arising from intrinsic structural instabilities – such as halide vacancies, ion migration and lattice defects, have hindered the transition of perovskite solar cells from laboratory prototypes to commercial modules. Among the various strategies explored to enhance stability, additive engineering and interfacial modifications have shown great promise, but scalable and efficient methods to reduce intrinsic defects within the perovskite lattice remain challenging. In this work, we present an oxygen-inducing strategy to fabricate metal halide perovskite thin films with increased performance. This approach not only improves the optoelectronic properties of the perovskite layer but also significantly enhances device stability under harsh testing conditions. Our findings offer insight into the role of oxygen in defect passivation and structural stabilization, providing a viable pathway toward more durable and commercially viable perovskite solar technologies.

Introduction

Metal halide perovskite-based solar cells are highly efficient photovoltaic (PV) systems with various appealing features such as low cost, excellent flexibility, portability, and color tunability, making them a next-generation PV technology.[1–5] Perovskite semiconductors show outstanding optoelectronic properties such as tunable bandgap, high absorption coefficients, long carrier diffusion length, low exciton binding energy, and high defect tolerance.[6–8] Notably, the efficiency of perovskite solar cells (PSCs) has now exceeded 26%.[9,10] The perovskite materials have a characteristic crystal structure with the chemical formula

---

[a] *Queensland Micro- and Nanotechnology Centre, School of Environment and Science, Griffith University, Nathan, Queensland 4111, Australia. E-mail: m.batmunkh@griffith.edu.au*

[b] *Center for Organic Photonics and Electronics Research (OPERA), Kyushu University, Fukuoka, 819-0395, Japan*

[c] *Adelaide Microscopy, The University of Adelaide, Adelaide, South Australia, 5005, Australia*

[d] *Department of Electronic and Electrical Engineering, University College London, Roberts Building, Torrington Pl, London, WC1E 7JE, UK*

[e] *London Centre for Nanotechnology, University College London, 19 Gordon St, London, WC1H 0AH, UK*

ABX_3, where A is a cation *e.g.*, MA^+: methylammonium, FA^+: formamidinium, or Cs^+; B is an inorganic metal cation (Pb^{2+} or Sn^{2+}); and X is a halide anion (I^-, Br^-, or Cl^-). In the early stage of development, methylammonium lead iodide ($MAPbI_3$) has been intensively explored in solar cell applications.[8,11–15] Despite the remarkable achievements, the volatile nature of MA^+ causes intrinsic poor thermal stability while the relatively large bandgap of $MAPbI_3$ limits its broad light absorption, both of which hinder its PV performances.[16–19]

Consequently, there has been growing interest in investigating alternative perovskite compositions with enhanced properties, with particular emphasis on the emerging alpha phase-pure formamidinium lead iodide (α-$FAPbI_3$).[20–22] With its low structural symmetry, the phase-pure α-$FAPbI_3$ has narrow bandgaps, allowing broad light absorption and approaching the ideal threshold for achieving high-performance solar cells.[23] Moreover, α-$FAPbI_3$ demonstrates excellent thermal stability compared to $MAPbI_3$ because of its extensive delocalized π bond and positive charges.[18] Therefore, phase-pure α-$FAPbI_3$ has been considered as a promising light-harvesting perovskite material for the record efficiency of PSCs.[21,24–27] Despite the great promise, photoactive black α-$FAPbI_3$ readily transforms into the undesired wide-bandgap yellow δ-phase with hexagonal symmetry under ambient conditions at room temperature.[18,28] This phase transition-related issue can be associated with several reasons such as halide vacancies, structural defects, ion migrations and others.[29,30] Over the past few years, extensive efforts have been made to enhance the efficiency and stability of PSCs using various strategies, including additive engineering,[31–35] surface passivation[5] and interfacial engineering.[4] For example, Cl^- anion additive engineering has been recognized as a simple and facile method to enhance stability, surface morphology, and crystallization growth while reducing structural defects.[31,33,35,36] Xie *et al.*[35] explored the role of MACl as an additive and showed that the Cl^- anion can promote the interaction between FA and I by passivating iodine vacancies in the crystal structure, achieving a vertically oriented crystal structure of perovskites with homogeneous grain morphology. Seok and colleagues have introduced a strategy to enhance stability by doping with methylenediammonium dichloride ($MDACl_2$), resulting in significant stability improvements.[34] Another promising additive engineering strategy is to use pseudo-halide anions with strong electronegativities, such as formate ($HCOO^-$) and acetate (CH_3COO^-), as they not only suppress halide vacancies but also improve crystal formation and growth.[22,24] Recently, Li's group fabricated highly efficient and stable PSCs in ambient air with the addition of guanabenz acetate salt, which is not limited to a glovebox and provides a feasible approach toward commercialization.[22] In an alternative approach, Du *et al.*[37] successfully converted yellow δ-$FAPbI_3$ into black α-$FAPbI_3$ using aerosol-assisted crystallization at 100 °C using precursor solutions containing only lead iodide and formamidinium iodide with no chemical additives.[38]

Meanwhile, recent studies have demonstrated that oxygen can effectively inhibit nonradiative recombination by bonding to halide vacancies in perovskite films.[39–46] For example, the photoluminescence (PL) intensity of $MAPbI_3$ increased by more than three orders of magnitude, and the corresponding PL lifetime was extended from just a few nanoseconds to hundreds of nanoseconds *via* oxygen passivation.[45] Subsequently, Liu *et al.*[44] systematically investigated the passivation effect of oxygen on $CsPbI_2Br$ using a combination of computational and experimental approaches. As a result, oxygen atom-passivated $CsPbI_2Br$-based (film annealed in air) PSCs exhibited higher power conversion efficiency (PCE) and enhanced stability as compared to the devices fabricated by annealing perovskite films in a N_2-filled glovebox. Despite this pioneering work, the role of oxygen in FA-based perovskites such as α-$FAPbI_3$ and FAMA-based PSCs still needs careful exploration to gain a better understanding.[21,47] More importantly, the primary method for achieving oxygen-passivated FA-based perovskite films involves annealing in ambient air, yet precise control of oxygen dosage remains to be explored. Excess oxygen can have detrimental effects by deprotonating organic cations, leading to degradation and reduced device performance.[39,48] Therefore, it is necessary to develop an effective and precise strategy to control the effect of oxygen in perovskite films for high efficiency and stable PSCs.

In this work, we carefully investigated the oxygen effect in FA-based metal halide perovskites by injecting oxygen into the precursor solution prior to the deposition and crystallization. A broad range of experimental measurements and theoretical calculations were carried out to elucidate the effect of oxygen on the structural, optical, electronic, and PV properties of metal halide perovskite thin films and solar cells. We anticipate that this work will not only demonstrate the feasibility of additive engineering using simple oxygen treatment in the perovskite precursor solution but also provide new knowledge in perovskite research.

Results and discussion

Fig. 1 illustrates the fabrication procedure of both reference (without oxygen) and target (with oxygen-induced) perovskite-based solar cells. A full description of the experimental procedure is provided in the SI. Briefly, a 1.4 M perovskite precursor solution was prepared by mixing α-$FAPbI_3$ powder (Fig. S1), $MDACl_2$ (3.8 mol%), and MACl (35 mol%) in a mixed solvent of DMF : DMSO and was filtered into sealable glass vials. Then, ultra-high purity (UHP) oxygen gas (1 mL for the target) was injected into the sealed glass vials containing perovskite precursor solutions (Fig. S2). It should be noted that the amount of injected oxygen was carefully controlled using a setup depicted in Fig. S3, where a syringe and a needle were placed as an outlet, and an oxygen gas-connected needle was inserted into the solution as an inlet. Then, the reference and oxygen-induced perovskite solutions were spin-coated onto the SnO_2 layer, followed by crystallization and deposition of hole-transporting layers (spiro-OMeTAD) and gold (Au) electrodes according to an established protocol.[34] Fig. S4 displays the cross-sectional scanning electron microscope (SEM) image of the full device with a layered structure of FTO/SnO_2/α-$FAPbI_3$/spiro-OMeTAD/Au. The thickness of the perovskite layer was measured to be ~450 nm, while having a flat and smooth contact with the spiro-

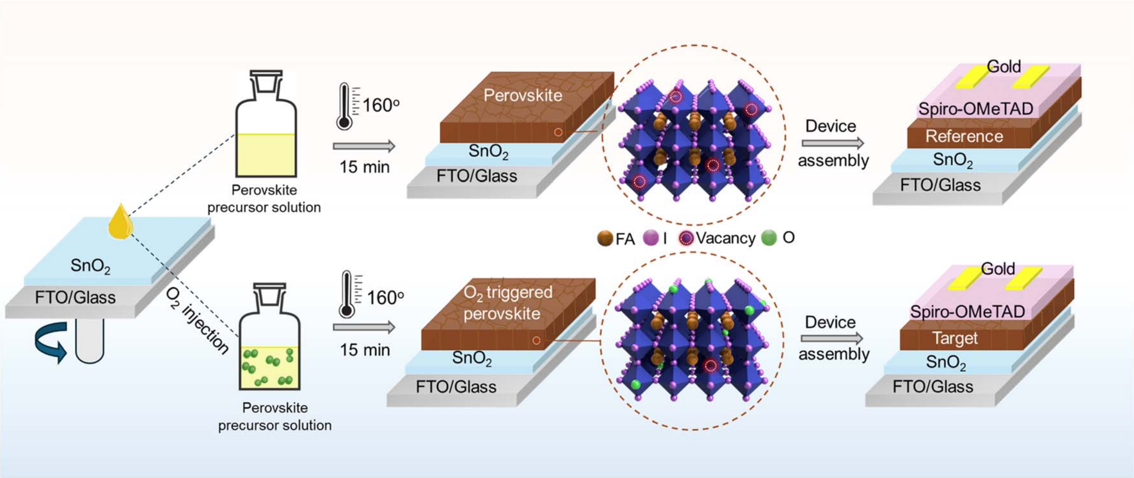

Fig. 1 Schematic illustration of the fabrication steps for the reference and target PSCs.

OMeTAD layer (180 nm thickness). Lastly, the thickness of SnO_2 and Au layers was ∼20 nm and ∼70 nm, respectively.

To study the structural and morphological characteristics of the reference and target films, a range of spectroscopic and microscopic techniques were used. Fig. 2a shows the X-ray diffraction (XRD) patterns of the reference and target perovskite thin films. The characteristic crystallographic planes of α-$FAPbI_3$ (001) and (002) were observed while a negligible PbI_2 peak was detected at 12.8° in both films. As shown in Fig. 2b, a sharp characteristic peak of α-$FAPbI_3$ (001) was observed at 14.15° with a calculated lattice parameter of 6.30 Å for the reference perovskite, which was consistent with previous literature.[29,35,47] In contrast, the (001) peak was shifted slightly to a lower angle (14.11°) for the target film with a lattice parameter of 6.32 Å. The same shift was also observed in the (002) plane (Fig. S5). These results suggest that the unit cell of the target perovskite expanded due to the presence of the oxygen atoms in the perovskite crystals, which will be discussed in detail later in accordance with our density-functional theory (DFT) calculations. Notably, this phenomenon was also observed in previous studies when other additives were introduced into the α-$FAPbI_3$ perovskite precursor solution.[34,35,49]

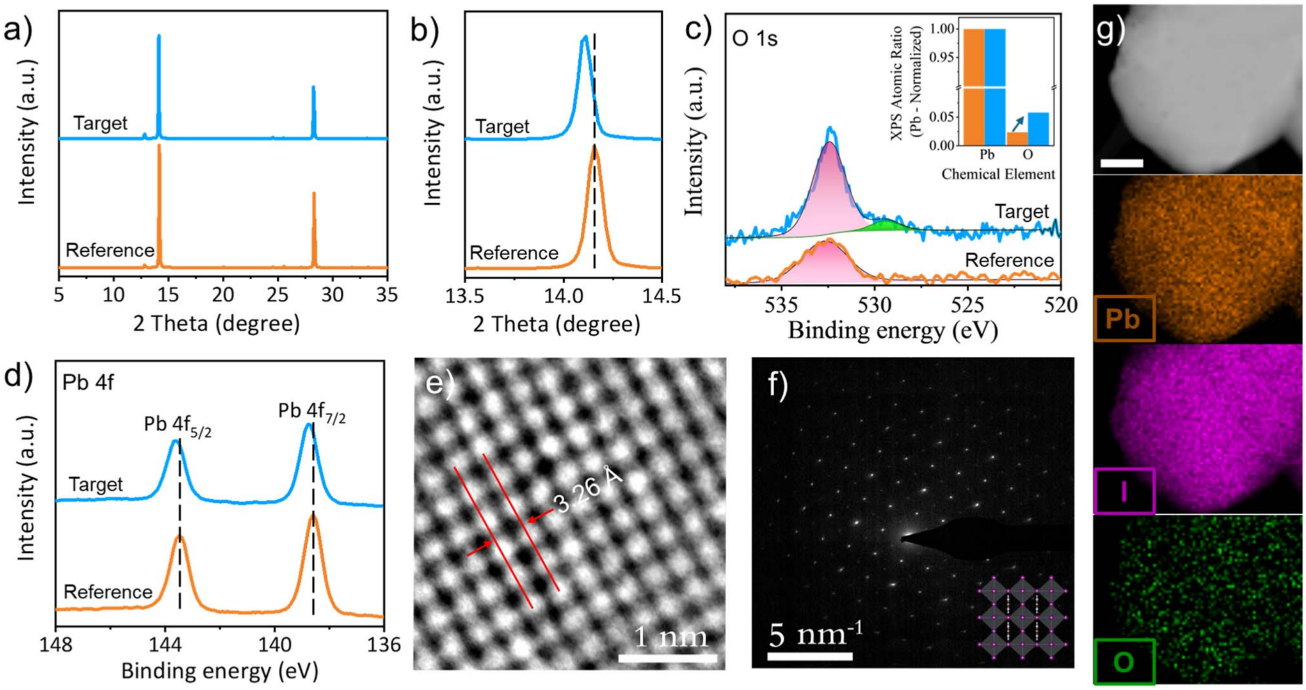

Fig. 2 (a) XRD patterns, (b) XRD patterns from 13.5 to 14.5°, (c) HR XPS O 1s spectra (inset shows the atomic ratio of oxygen normalized to lead (Pb 4f) peak intensity) and (d) XPS Pb 4f spectra of the reference and target perovskite films. (e) HRTEM image, (f) SAED pattern, (g) HAADF-STEM (scale bar: 200 nm), and the corresponding elemental mapping images of the target perovskite film.

Furthermore, we explored the chemical structure and spatial distribution of oxygen-induced perovskite samples using X-ray photoelectron spectroscopy (XPS). The survey scans of both samples were identical (Fig. S6). High resolution (HR) XPS O 1s spectra of both films exhibited peaks at a binding energy of around 532 eV (depicted in Fig. 2c), corresponding to adsorbed oxygen in the molecular state of both samples as they were crystallized in ambient air with a relative humidity (RH) of 30–40%.[44] Interestingly, it can be observed from the inset of Fig. 2c that the calculated O/Pb peak intensity ratio increased from 0.024 to 0.058 atomic content after oxygen induction into the perovskite precursor. More importantly, an additional peak observed at 528.6 eV only appeared in the target film, corresponding to the presence of atomically bonded oxygen with the neighbouring atom (Pb), as it was observed in the literature.[44,50] Furthermore, Fig. 2d displays the HR XPS Pb 4f spectra of both reference and target perovskite films, which can be deconvoluted into one main doublet with a splitting of 4.86 eV.[47] These peaks correspond to the Pb $4f_{7/2}$ and Pb $4f_{5/2}$ doublet associated with Pb-halide bonding, indicating the absence of any metallic Pb^0 peak. As shown in Fig. 2d, the Pb $4f_{7/2}$ and Pb $4f_{5/2}$ peaks of the target (1 mL oxygen injected) sample were located at slightly higher binding energies as compared to the reference perovskite without any oxygen-inducing effect. According to the XPS handbook,[51] this shift (0.2 eV) to the higher binding energy indicates that oxygen introduced in the target perovskite bonded with Pb as a halide, confirming the passivation of halide vacancies. When the amount of oxygen increased (from 1 mL to 4 mL), there were noticeable shifts to the lower binding energies in the Pb 4f peaks (Fig. S7). This suggests that the high amount of oxygen introduction into the perovskite leads to the formation of Pb–O bonds instead of passivating halide vacancies. Both XRD and XPS results confirm that we have successfully passivated the halide vacancies in α-$FAPbI_3$ films through a precisely controlled oxygen-inducing effect into the perovskite precursor solution.

The crystal structure of the as-prepared thin films was investigated using high resolution transmission electron microscopy (HRTEM) and selected-area electron diffraction (SAED) patterns. Fig. 2e and S8 display the HRTEM image of the target and reference perovskite films, where the lattice spacing can be measured to be ≈3.26 Å and ≈3.20 Å, respectively, which agrees with the (002) lattice planes of the α-$FAPbI_3$ cubic phase.[52] The corresponding SAED pattern in Fig. 2f displays a series of sharp diffraction spots which can be correlated to the cubic perovskite crystal structure with a space group *Pm*-3*m*, $a = b = c = 6.41$ Å , and $\alpha = \beta = \gamma = 90°$.[52] This suggests that the oxygen-induced perovskite film has a preferred (001) crystallographic orientation along the crystal growth direction, confirming that this simple strategy did not deteriorate the crystal structure of α-$FAPbI_3$. Moreover, the Time-of-Flight Secondary Ion Mass Spectrometry (ToF-SIMS) profile of the perovskite films studied, as shown in Fig. S9, highlights that no notable differences in PbO^- or PbI_2^- ion concentrations are observed between the reference and target samples. Furthermore, the accompanying 3D ion distribution renders (Fig. S10) confirm comparable spatial distributions of PbO^- and PbI_2^- for both sets of films. This indicates the absence of excess lead oxide or iodide in the target films, thus corroborating the phase purity of the synthesized perovskite films consistent with the SAED patterns.[53,54] The chemical compositions of the perovskite films were studied using high-angle annular dark-field-scanning transmission electron microscopy (HAADF-STEM) measurements with selected elemental mapping images (Fig. 2g and S11). As shown in Fig. 2g, elemental mapping images suggest that the target film consists of Pb and I with a small amount of O.

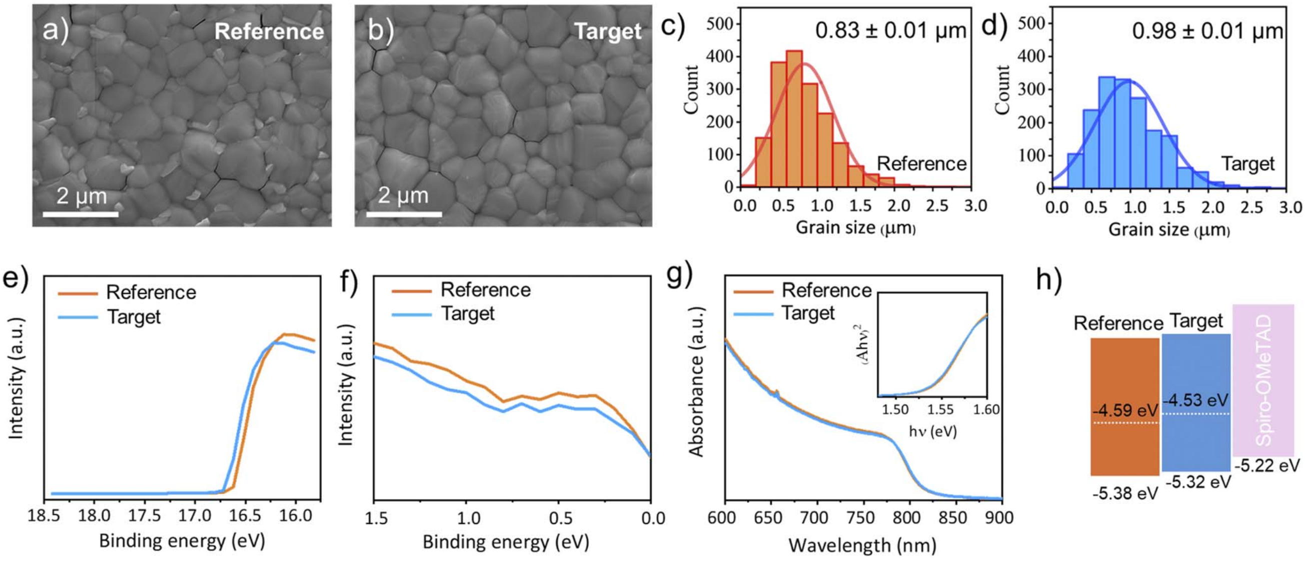

Fig. 3 (a) and (b) Top-view SEM images, (c) and (d) grain size distribution measurements, (e) and (f) UPS spectra, (g) UV-vis spectra (inset shows the Tauc plot) of the reference and target perovskite films, and (h) the calculated energy level diagram and Fermi level of the perovskite films and spiro-OMeTAD.

The surface morphology of the perovskite films was evaluated using top-view scanning electron microscopy (SEM), which showed similar well-organized pinhole-free grains for the reference (Fig. 3a) and target (Fig. 3b) films. Notably, it can be seen from Fig. 3c and d that the average grain size of the reference and target films was measured to be 0.83 ± 0.01 μm and 0.98 ± 0.01 μm, respectively. This suggests that the oxygen injection promoted homogeneous crystallization while reducing the amount of PbI_2 on the surface of the perovskite grains (Fig. S12).

To gain an in-depth understanding of the electronic properties of the perovskites, ultraviolet photoelectron spectroscopy (UPS) and ultraviolet-visible (UV-vis) absorption were carried out. The energy level alignments of perovskite films were acquired from both UPS data analysis (Fig. 3e and f) and bandgap calculations (Fig. 3g). In particular, the valence band maximum (VBM) and conduction band minimum (CBM) were slightly up-shifted for α-$FAPbI_3$ with oxygen injection, suggesting better suitability with the energy level of the hole transporting layer (spiro-OMeTAD). As shown in Fig. 3g, no change was observed in the UV-vis spectra of both films. The calculated bandgaps of both α-$FAPbI_3$ films were 1.54 eV (Fig. 3g inset), which is in excellent agreement with the literature.[47] Thus, this suitable energy alignment is expected to lead to improved charge extraction and reduced charge recombination in the fabricated solar cells (Fig. 3h).

To further investigate the effect of oxygen on the PV performance of α-$FAPbI_3$ perovskite solar cells, the devices with a configuration of fluorine-doped tin oxide (FTO)/SnO_2/α-$FAPbI_3$/spiro-OMeTAD/Au were fabricated and their PV parameters were measured under 1 sun (AM 1.5G) solar illumination. Fig. 4a–d presents the detailed PV parameters, including V_{oc}, fill factor (FF), short-circuit current (J_{sc}), and PCE. The photocurrent–voltage (J–V) curves of the best-performing PSCs are shown in Fig. 4e. The oxygen-induced α-$FAPbI_3$-based PSCs achieved a PCE of 21.33% with a V_{oc} of 1.073 V, J_{sc} of 26.03 mA cm^{-2}, and FF of 78.5, which were higher than the reference device with a PCE of 20.33%, V_{oc} of 1.057 V, J_{sc} of 25.84 mA cm^{-2} and FF of 74.4. In particular, the improved V_{oc} and FF values are attributed to the suitable energy level alignment of the target perovskite film with spiro-OMeTAD (Fig. 3h), allowing efficient photogenerated hole transport. We also observed the same trends of enhanced V_{oc} and FF for the PSCs fabricated with α-$FAPbI_3$ and different metal halide perovskite (FAMA) crystallized in a N_2-filled glovebox (Fig. S13 and S14).

As shown in Fig. 4f, the external quantum efficiency (EQE) spectra of both reference and target devices were similar, displaying excellent light absorption and conversion efficiencies at wavelengths ranging from 350 nm to 850 nm. The integrated J_{sc} values from the EQE spectra were 24.2 mA cm^{-2} and 24.5 mA cm^{-2} for the reference and target devices, respectively, both of which are in the range of the corresponding statistical distribution of the measured J_{sc} values. As illustrated in Fig. 4g, the statistical PCE distribution of 30 devices for each reference and target PSC demonstrated the high reproducibility and repeatability of oxygen-induced α-$FAPbI_3$-based devices *versus* reference devices. The device efficiencies vary between 16.75% and 20.25% for the reference and 18.75% to 21.33% for the target cells. This can be considered as a noticeable improvement for α-$FAPbI_3$-based devices, as this strategy reduces the influence of environmental factors, particularly RH in ambient air. It should be noted that we have carried out detailed investigations to understand the effect of different amounts of oxygen in the α-$FAPbI_3$ perovskite (Fig. S15). It can be seen from Fig. S16 that the PV parameters of PSCs are dependent on the volume of oxygen injected into the precursor solution. The devices with 0.5 mL showed improved PCE values as compared to the reference cells (0 mL). However, the reductions in the PV performances of the PSCs with more than 1 mL are due to the formation of Pb–O as demonstrated previously by our XPS measurements (Fig. S7).

To have a better understanding of the role of oxygen-inducing effect, we have carried out electrochemical impedance spectroscopy (EIS) measurements of the fabricated devices under ambient conditions and light illumination. The EIS technique was applied to study the electrical and ionic charge dynamics in the fabricated devices. As depicted in Fig. 4h, the obtained data were fitted with ZView using an equivalent circuit model shown in the inset. The Nyquist plots show one semicircle, which is a typical EIS response for planar n-i-p devices. The circuit consists of a series resistance (R_s) and a charge recombination resistance (R_{rec}) with a double-layer capacitance (C_{dl}).[55,56] The R_s mainly occurred at the FTO/SnO_2 interface, while R_{rec} was associated with the perovskite/spiro-OMeTAD interface due to charge recombination. Both reference and target devices had similar R_s values as shown in Table S1, but the R_{rec} value of the target devices (446.5 Ω cm^{-2}) was considerably higher than that of the reference devices (262.7 Ω cm^{-2}). The increased R_{rec} indicates that the oxygen-inducing effect on α-$FAPbI_3$ reduced the charge recombination at the perovskite/spiro-OMeTAD interface due to the favourable energy alignment. Furthermore, steady-state PL and time-resolved PL (TRPL) measurements were carried out to study the nonradiative recombination of the perovskite films. An excitation wavelength of 355 nm was applied to the glass side of the films. The PL intensity of the target film was considerably higher than that of the reference film, implying reduced nonradiative recombination in the oxygen-induced α-$FAPbI_3$ film (Fig. 4i). Time-correlated single-photon counting was used to acquire a more quantitative understanding of charge kinetics. The corresponding average bi-exponential lifetimes in Table S2 were calculated from the PL decay curves, as illustrated in Fig. 4j. The film with oxygen-induced α-$FAPbI_3$ showed a longer lifetime (102.5 ns) than the α-$FAPbI_3$ film without oxygen (73.7 ns). Hence, the higher PL intensity and longer lifetime in the target film suggest reduced defects and suppressed nonradiative charge recombination, which are critical for achieving excellent PV performance and stability of solar cells.

Considering the better performance of oxygen-induced PSCs, we then tested their stability under three different conditions based on the International Summit on Organic Photovoltaic Stability (ISOS) protocols.[57] First, PSCs with and without oxygen-inducing effect were stored in a nitrogen atmosphere and annealed at a temperature of 85 °C. Both devices were stable in an inert atmosphere. The target device showed slightly better

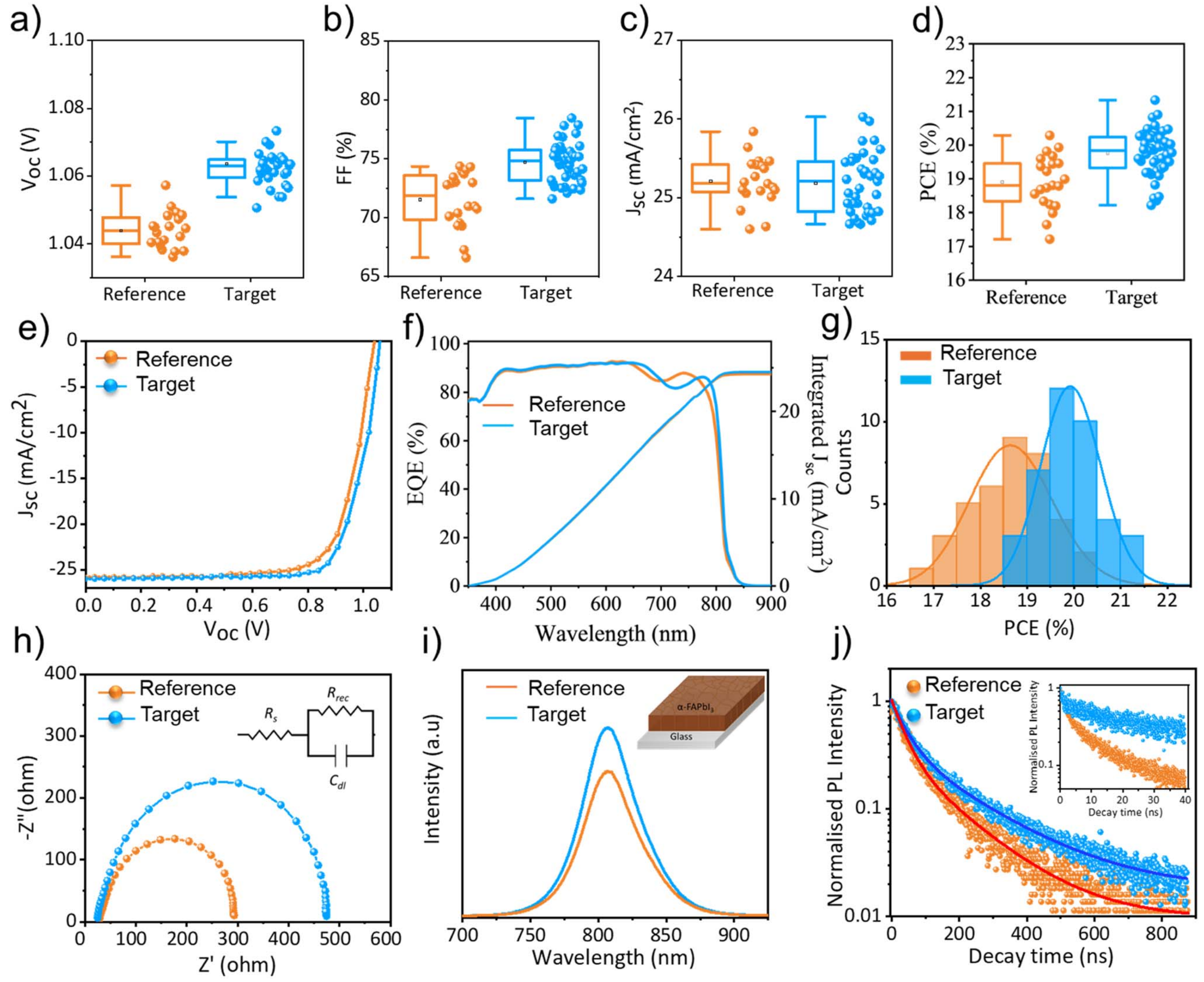

Fig. 4 Statistical distribution of the PV parameters (a) V_{OC}, (b) FF, (c) J_{SC} and (d) PCE of reference and target (oxygen-induced) perovskite-based solar cells. (e) J–V characteristics and (f) EQE spectra of the best-performing devices. (g) PCE of 30 devices for each device type of the reference and target PSCs. (h) EIS Nyquist plots of the best-performing reference and target devices. (i) PL spectra and (j) TRPL decays of perovskite films.

stability, retaining 92% of its initial value, while the reference device retained 86% of the initial PCE (Fig. 5a). This slight improvement could be attributed to the mitigation of iodine migration from α-FAPbI$_3$ to spiro-OMeTAD by passivating halide vacancies with oxygen atoms. It has been reported that iodine migration from perovskite into the HTM shows an adverse effect on PV performance and stability, particularly at higher temperatures.[58–60] To compare the iodine migration of both reference and target perovskite films, the films were immersed in glass vials containing anhydrous toluene and heated at 85 °C for 1 h (Fig. S17). The color of the toluene solution turned pink after heating at 85 °C for 1 h, while the solution color remained unchanged at 25 °C after 1 h. This color change is due to the iodine migration from the perovskite. The UV-vis spectra reveal that the iodine release from both films was similar at 25 °C, but the iodine migration increased after heating at 85 °C. It is noteworthy that oxygen-induced perovskite film showed slightly lower UV-vis spectrum intensity than the reference sample, confirming a slight improvement in stability, as shown in Fig. 5a.

Then, we tested device stability by annealing the devices at 85 °C under humid conditions (85% RH), as illustrated in Fig. 5b. The target device retained 74% of the PCE relative to its initial value, whereas the reference device showed 47% decay of the PCE after being heated at 85 °C in 85% RH for 360 min. The improved stability under these harsh conditions suggests that oxygen atom passivation prevents perovskite films from moisture by increasing the hydrophobicity of the perovskite surface. Next, a long-term stability test was conducted on both devices (unencapsulated) under ambient conditions (∼50–75% RH) for 30 days (Fig. 5c). The efficiency of the reference device retained only 7.7% of its initial value, while the target device retained 46.6% of the initial PCE, suggesting that oxygen-induced perovskite has higher suppression of the defects at the

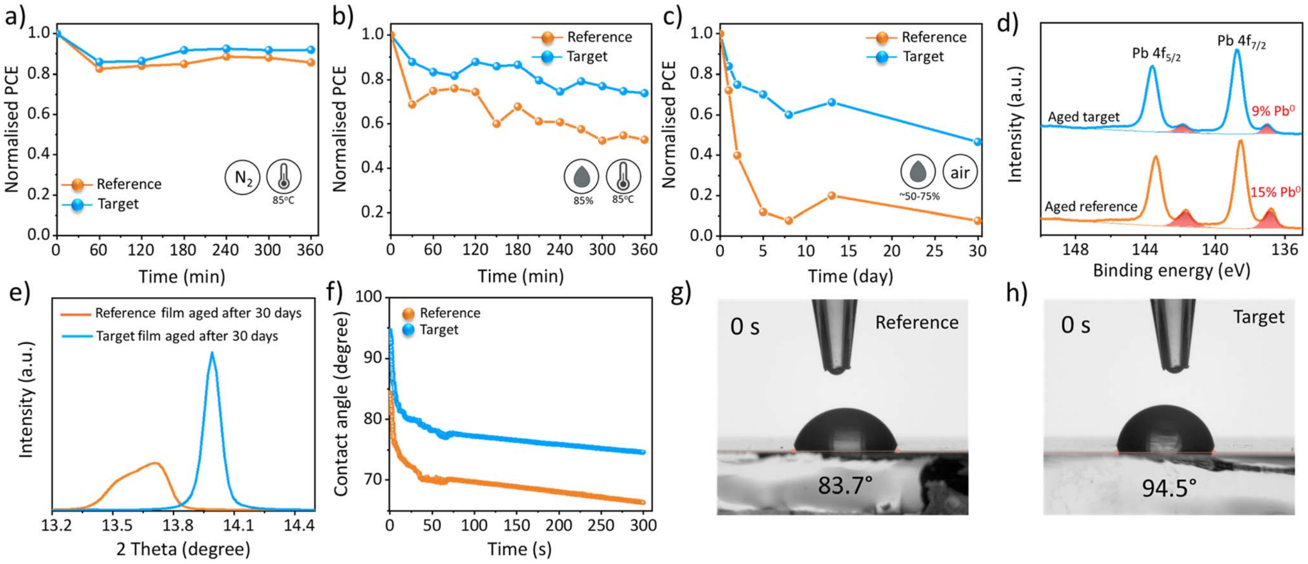

Fig. 5 Stability tests of unencapsulated PSCs with and without oxygen-induced perovskite aged (a) at 85 °C in an N_2 atmosphere, (b) at 85 °C and 85% RH for 360 min, and (c) under ambient conditions with ~50–75% RH for 30 days. (d) XPS HR Pb 4f spectra of aged reference and target films at ~85% RH for 360 min. (e) XRD patterns of the perovskite films aged for 30 days. (f) Average contact angle measurements of the reference and target perovskite films over 300 s. Photograph of contact angle measurements of the water droplet on the (g) reference and (h) target perovskite films.

perovskite/HTM interface with improved moisture resistance. Moreover, we investigated the chemical composition of the perovskite films using XPS measurements after aging them at 85% RH for 360 min. Unlike freshly prepared perovskite films, metallic Pb^0 peaks were observed in the HR Pb 4f spectra of the aged films. The calculated Pb^0 and Pb^{2+} ratio was 15% and 9% for the aged reference and target films, respectively, as shown in Fig. 5d. Furthermore, the characteristic XRD peak assigned to the 001 plane of the aged target perovskite film remained unchanged, whereas the reference α-$FAPbI_3$ thin film shifted to the lower angle with broader and reduced intensity after storing under ambient conditions for more than 30 days (Fig. 5e). These results reveal that the oxygen-induced α-$FAPbI_3$ film is structurally more stable and water tolerant than the reference α-$FAPbI_3$ film.

To confirm the stability improvements, the water droplet contact angles of reference and target perovskite films were measured over 300 seconds, as shown in Fig. 5f. It can be seen from Fig. 5g and h that the initial contact angles of the reference and target films were 83.7° and 94.5°. However, after 300 seconds, the contact angle values of the reference and target films decreased to 66.3° and 74.5°, respectively. These results confirm that oxygen passivation enhances the film hydrophobicity and thus improves the moisture resistance of the perovskite films. Therefore, these stability tests and contact angle measurements confirm that oxygen atoms can effectively passivate halide vacancies and enhance water tolerance, resulting in stable PSCs. The strategy developed in this work may hold great promise for the fabrication of large-area perovskite solar cells *via* a roll-to-roll fabrication method. However, a precise process control at industrial throughputs and effective mitigation of oxidative side effects should be carefully considered.

DFT calculations were performed to provide a better understanding of the structural and electronic properties of α-$FAPbI_3$ passivated with oxygen using the VASP package.[61,62] The details of the computational procedure are described in the SI. First, we examined the changes in unit cell lattice parameters for α-$FAPbI_3$ with a halide vacancy (called v_$FAPI_3$) and the oxygen-passivated α-$FAPbI_3$ (called O_$FAPI_3$). The optimized structures and lattice parameters of v_$FAPI_3$ and O_$FAPI_3$ are shown in the SI, Fig. S18. DFT optimizations show that the volume of unit cells has been increased from 214 Å^3 for v-$FAPI_3$ to 227 Å^3 for O_$FAPI_3$ upon passivating with oxygen. This observation supports the XRD analysis in Fig. 2b, wherein the shift of the (001) peak to a lower value suggested the expansion of the unit cell upon incorporating oxygen atoms at halide vacancies in the lattice.

Next, we studied the surface structure of O_$FAPI_3$ at different dosages of oxygen. Two scenarios are evaluated, including the incorporation of oxygen atoms at one halide vacancy site to reflect the low dosage of oxygen, and the incorporation of oxygen atoms at two adjacent halide vacancy sites to represent the high dosage of oxygen. A similar approach was also successfully applied to study the low and high coverages of polyols on transition metals by Trinh *et al.*[63] In the first case, at one vacancy site, there are two possible configurations for incorporating oxygen atoms. Oxygen could be adsorbed in the molecular structure (Fig. 6a) or in the dissociated atomic configuration (Fig. 6b), with the latter being 68 kJ mol^{-1} more stable. The activation barrier for O_2 dissociation from molecular adsorption is 54 kJ mol^{-1} (Fig. S19), indicating that the formation of atomic oxygen incorporation into the halide

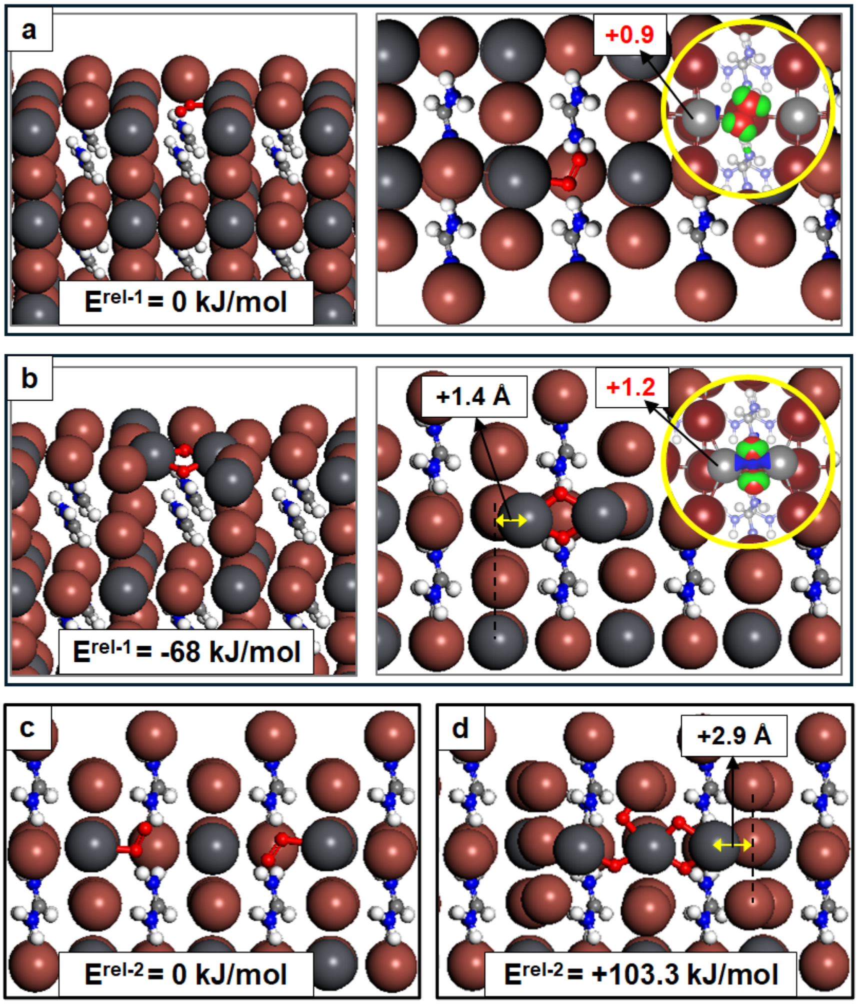

Fig. 6 (a) Side view (left) and top view (right) of molecular adsorption of O_2 at one halide vacancy site. (b) Side view (left) and top view (right) of atomic adsorption of O atoms at one halide vacancy site. The inserted images in Fig. 6a and b are the charge density difference (CDD) plots, wherein excessive and deficit electron densities are presented by green and blue regions, respectively. Charges of Pb atoms coordinating with oxygen atoms are shown in red color. Relative energy to the total molecular adsorption (Fig. 6a) is indicated by $E^{\mathrm{rel}-1}$ values. Top view of (c) molecular adsorption of O_2 and (d) atomic adsorption of O atoms at two adjacent halide vacancy sites. Relative energy to the total molecular adsorption (Fig. 6c) is indicated by $E^{\mathrm{rel}-2}$ values. The shifting distance of Pb atoms from the original positions (dashed line) is presented in Fig. 6b and d.

vacancy site is both thermodynamically and kinetically favorable *via* the annealing treatment in this study. A similar configuration was also reported for oxygen passivation in $CsPbI_2Br$.[44] Further examination of electronic properties *via* charge density difference (CDD) plots shows that there is only weak charge transfer between the adsorbed O_2 molecule and the coordinating Pb site in Fig. 6a, while much stronger charge transfer between oxygen atoms and Pb sites occurs in Fig. 6b, which is reflected from the presence of deficit electron densities along the Pb–Pb atoms (blue colour region in Fig. 6b). This strong charge transfer induces a positive charge on Pb atoms of +1.2 for the dissociative atomic oxygen incorporated configuration, as compared with a charge of +0.9 for the Pb atom in the molecular adsorption of O_2 (Fig. 6a). It should be mentioned that the molecular adsorption of oxygen at the halide vacancy site (Fig. 6a) resembles the resilient surface oxygen when α-$FAPbI_3$ is exposed to the air atmosphere and could be used to represent the reference sample, while the dissociated atomic oxygen adsorption could be used to represent the target sample in Fig. 2d. The more positive charge induced on surface Pb atoms upon passivating with oxygen is therefore greatly consistent with the shift of HR XPS Pb 4f peaks[47,64,65] at a low dosage of oxygen as is shown in Fig. 2d. It is also important to note that in the dissociated atomic configuration (Fig. 6b), slight surface reconstruction occurs and Pb atoms are shifted by ~1.4 Å from their original positions in the reference sample.

In the second case, when oxygen atoms are incorporated at two adjacent halide vacancy sites that represent the higher dosage of oxygen, the relative stability between the molecular adsorption and the dissociative atomic oxygen configuration is reversed. The molecular adsorption of O_2 at two adjacent vacancy sites (Fig. 6c) is 103 kJ mol^{-1} and is more stable than the dissociative atomic oxygen configuration (Fig. 6d). The instability of the dissociative atomic oxygen configuration is due to the severe reconstruction of surface Pb atoms. Indeed, to incorporate the dissociative oxygen atoms at two adjacent vacancy sites, Pb atoms must be shifted by ∼2.9 Å from their original positions, which requires a large extra energy penalty to drive this reconstruction.[66–68] Therefore, at a high dosage of oxygen passivation, the molecular adsorption configuration is likely to be dominated and does not result in modification of the electronic properties of passivated α-$FAPbI_3$. This explains the shift of the HR XPS Pb 4f peaks back to lower binding energies at higher oxygen dosages in Fig. S7. Finally, water adsorption on v-$FAPI_3$ and O_$FAPI_3$ is also investigated, and the optimized structures are shown in the SI, Fig. S20. The adsorption energies of H_2O on v-$FAPI_3$ and O_$FAPI_3$ are −57 and −41 kJ mol^{-1}, respectively. Due to the weaker adsorption of H_2O, O_$FAPI_3$ is more hydrophobic and has more resistance to moisture attack, explaining its higher stability and better performance under the humidity test, as shown in Fig. 5.

Conclusions

In summary, we have investigated the oxygen-inducing effect in phase-pure α-$FAPbI_3$ and its solar cells by controllably injecting oxygen into the perovskite precursor solution. We found that oxygen-induced PSCs performed better than devices without oxygen, achieving improved V_{oc}, FF, and PCE values. Notably, these improvements are due to the suitable energy alignment with the hole transporting layer and reduced nonradiative charge recombination, as evidenced by various spectroscopic and microscopic techniques. Along with their excellent PV performance, the unencapsulated devices fabricated with oxygen-induced perovskites showed remarkable stabilities under various harsh testing conditions, including high temperature and humidity, suggesting that an accurate amount of oxygen passivation could stabilize the perovskite structure while increasing the water tolerance of the α-$FAPbI_3$ structure.

Author contributions

S. S. and M. B. conceived the project idea. M. B. supervised the project. S. S. fabricated and characterized devices, validated the results, visualized the data, and wrote the first draft of the manuscript. P. M., A. A, S. P. and E. C. contributed to the materials preparation and device fabrication. Q. T. T., T. G. and N. T. N. carried out the computational calculations. T. T. and C. A. supported with PL and TRPL measurements. A. D. S. carried out the HRTEM analysis. O. E. F., T. J. Z. S. and T. J. M carried out the ToF-SIMS measurements. S. J and Y. L. Z. contributed to the project discussion, data analysis and validation.

Conflicts of interest

There are no conflicts to declare.

Data availability

The data supporting this article have been included as part of the SI. See DOI: **https://doi.org/10.1039/d5el00098j**.

Acknowledgements

This work was financially supported by the Australian Research Council (DE220100521). This work used the Queensland node of the NCRIS-enabled Australian National Fabrication Facility (ANFF). The authors gratefully acknowledge the use of the Centre for Microscopy and Microanalysis (CMM) facilities at the University of Queensland, Australia. S. S., A. A., and S. P. would like to acknowledge the financial support of the Griffith University International Postgraduate Research Scholarship (GUIPRS) and Griffith University Postgraduate Research Scholarship (GUPRS). Q. T. T. and N-T. N. would like to acknowledge the financial support by the Australian Research Council (FL230100023). Q. T. T. and T. G. acknowledge the computational support from the Australian National Computing Initiative through the NCMAS project sp13 and the Griffith University Gowonda HPC Cluster for using computational resources. T. T. and C. A. acknowledge the financial support from JST CREST (grant no. JPMJCR22B3) and JSPS KAKENHI International Leading Research (ILR) (23K20039).

References

1 A. S. R. Bati, Y. L. Zhong, P. L. Burn, M. K. Nazeeruddin, P. E. Shaw and M. Batmunkh, *Commun. Mater.*, 2023, **4**, 2.

2 S. Suragtkhuu, S. Sunderiya, P. Myagmarsereejid, S. Purevdorj, A. S. R. Bati, B. Bold, Y. L. Zhong, S. Davaasambuu and M. Batmunkh, *Adv. Energy Mater.*, 2023, **13**, 2204074.

3 M. Batmunkh, Y. L. Zhong and H. Zhao, *Adv. Mater.*, 2020, **32**, 2000631.

4 J. Kong, Y. Shin, J. A. Röhr, H. Wang, J. Meng, Y. Wu, A. Katzenberg, G. Kim, D. Y. Kim, T.-D. Li, E. Chau, F. Antonio, T. Siboonruang, S. Kwon, K. Lee, J. R. Kim, M. A. Modestino, H. Wang and A. D. Taylor, *Nature*, 2021, **594**, 51–56.

5 Q. Jiang, Y. Zhao, X. Zhang, X. Yang, Y. Chen, Z. Chu, Q. Ye, X. Li, Z. Yin and J. You, *Nat. Photon.*, 2019, **13**, 460–466.

6 J.-P. Correa-Baena, A. Abate, M. Saliba, W. Tress, T. Jesper Jacobsson, M. Grätzel and A. Hagfeldt, *Energy Environ. Sci.*, 2017, **10**, 710–727.

7 G. E. Eperon, T. Leijtens, K. A. Bush, R. Prasanna, T. Green, J. T.-W. Wang, D. P. McMeekin, G. Volonakis, R. L. Milot, R. May, A. Palmstrom, D. J. Slotcavage, R. A. Belisle, J. B. Patel, E. S. Parrott, R. J. Sutton, W. Ma, F. Moghadam, B. Conings, A. Babayigit, H.-G. Boyen, S. Bent, F. Giustino, L. M. Herz, M. B. Johnston, M. D. McGehee and H. J. Snaith, *Science*, 2016, **354**, 861–865.

8 N. J. Jeon, J. H. Noh, W. S. Yang, Y. C. Kim, S. Ryu, J. Seo and S. I. Seok, *Nature*, 2015, **517**, 476–480.

9 S. Liu, J. Li, W. Xiao, R. Chen, Z. Sun, Y. Zhang, X. Lei, S. Hu, M. Kober-Czerny, J. Wang, F. Ren, Q. Zhou, H. Raza, Y. Gao,

Y. Ji, S. Li, H. Li, L. Qiu, W. Huang, Y. Zhao, B. Xu, Z. Liu, H. J. Snaith, N.-G. Park and W. Chen, *Nature*, 2024, **632**, 536–542.

10 Y. Yang, H. Chen, C. Liu, J. Xu, C. Huang, C. D. Malliakas, H. Wan, A. S. R. Bati, Z. Wang, R. P. Reynolds, I. W. Gilley, S. Kitade, T. E. Wiggins, S. Zeiske, S. Suragtkhuu, M. Batmunkh, L. X. Chen, B. Chen, M. G. Kanatzidis and E. H. Sargent, *Science*, 2024, **386**, 898–902.

11 J. Burschka, N. Pellet, S.-J. Moon, R. Humphry-Baker, P. Gao, M. K. Nazeeruddin and M. Grätzel, *Nature*, 2013, **499**, 316–319.

12 J.-H. Im, C.-R. Lee, J.-W. Lee, S.-W. Park and N.-G. Park, *Nanoscale*, 2011, **3**, 4088–4093.

13 H.-S. Kim, C.-R. Lee, J.-H. Im, K.-B. Lee, T. Moehl, A. Marchioro, S.-J. Moon, R. Humphry-Baker, J.-H. Yum, J. E. Moser, M. Grätzel and N.-G. Park, *Sci. Rep.*, 2012, **2**, 591.

14 A. Kojima, K. Teshima, Y. Shirai and T. Miyasaka, *J. Am. Chem. Soc.*, 2009, **131**, 6050–6051.

15 H. Zhou, Q. Chen, G. Li, S. Luo, T.-b. Song, H.-S. Duan, Z. Hong, J. You, Y. Liu and Y. Yang, *Science*, 2014, **345**, 542–546.

16 E. J. Juarez-Perez, Z. Hawash, S. R. Raga, L. K. Ono and Y. Qi, *Energy Environ. Sci.*, 2016, **9**, 3406–3410.

17 B. Conings, J. Drijkoningen, N. Gauquelin, A. Babayigit, J. D'Haen, L. D'Olieslaeger, A. Ethirajan, J. Verbeeck, J. Manca, E. Mosconi, F. D. Angelis and H.-G. Boyen, *Adv. Energy Mater.*, 2015, **5**, 1500477.

18 C. C. Stoumpos, C. D. Malliakas and M. G. Kanatzidis, *Inorg. Chem.*, 2013, **52**, 9019–9038.

19 T. J. Macdonald, A. J. Clancy, W. Xu, Z. Jiang, C.-T. Lin, L. Mohan, T. Du, D. D. Tune, L. Lanzetta, G. Min, T. Webb, A. Ashoka, R. Pandya, V. Tileli, M. A. McLachlan, J. R. Durrant, S. A. Haque and C. A. Howard, *J. Am. Chem. Soc.*, 2021, **143**, 21549–21559.

20 M. Kim, J. Jeong, H. Lu, T. K. Lee, F. T. Eickemeyer, Y. Liu, I. W. Choi, S. J. Choi, Y. Jo, H.-B. Kim, S.-I. Mo, Y.-K. Kim, H. Lee, N. G. An, S. Cho, W. R. Tress, S. M. Zakeeruddin, A. Hagfeldt, J. Y. Kim, M. Grätzel and D. S. Kim, *Science*, 2022, **375**, 302–306.

21 J. Park, J. Kim, H.-S. Yun, M. J. Paik, E. Noh, H. J. Mun, M. G. Kim, T. J. Shin and S. I. Seok, *Nature*, 2023, **616**, 724–730.

22 L. Yan, H. Huang, P. Cui, S. Du, Z. Lan, Y. Yang, S. Qu, X. Wang, Q. Zhang, B. Liu, X. Yue, X. Zhao, Y. Li, H. Li, J. Ji and M. Li, *Nat. Energy*, 2023, **8**, 1158–1167.

23 S. Tan, T. Huang, I. Yavuz, R. Wang, M. H. Weber, Y. Zhao, M. Abdelsamie, M. E. Liao, H.-C. Wang, K. Huynh, K.-H. Wei, J. Xue, F. Babbe, M. S. Goorsky, J.-W. Lee, C. M. Sutter-Fella and Y. Yang, *J. Am. Chem. Soc.*, 2021, **143**, 6781–6786.

24 J. Jeong, M. Kim, J. Seo, H. Lu, P. Ahlawat, A. Mishra, Y. Yang, M. A. Hope, F. T. Eickemeyer, M. Kim, Y. J. Yoon, I. W. Choi, B. P. Darwich, S. J. Choi, Y. Jo, J. H. Lee, B. Walker, S. M. Zakeeruddin, L. Emsley, U. Rothlisberger, A. Hagfeldt, D. S. Kim, M. Grätzel and J. Y. Kim, *Nature*, 2021, **592**, 381–385.

25 H. Min, S.-G. Ji and S. I. Seok, *Joule*, 2022, **6**, 2175–2185.

26 H.-S. Yun, H. W. Kwon, M. J. Paik, S. Hong, J. Kim, E. Noh, J. Park, Y. Lee and S. Il Seok, *Nat. Energy*, 2022, **7**, 828–834.

27 Y. Zhao, F. Ma, Z. Qu, S. Yu, T. Shen, H.-X. Deng, X. Chu, X. Peng, Y. Yuan, X. Zhang and J. You, *Science*, 2022, **377**, 531–534.

28 O. J. Weber, D. Ghosh, S. Gaines, P. F. Henry, A. B. Walker, M. S. Islam and M. T. Weller, *Chem. Mater.*, 2018, **30**, 3768–3778.

29 N. Li, Y. Luo, Z. Chen, X. Niu, X. Zhang, J. Lu, R. Kumar, J. Jiang, H. Liu, X. Guo, B. Lai, G. Brocks, Q. Chen, S. Tao, D. P. Fenning and H. Zhou, *Joule*, 2020, **4**, 1743–1758.

30 S.-H. Turren-Cruz, A. Hagfeldt and M. Saliba, *Science*, 2018, **362**, 449–453.

31 M. Kim, G.-H. Kim, T. K. Lee, I. W. Choi, H. W. Choi, Y. Jo, Y. J. Yoon, J. W. Kim, J. Lee, D. Huh, H. Lee, S. K. Kwak, J. Y. Kim and D. S. Kim, *Joule*, 2019, **3**, 2179–2192.

32 S. Yang, W. Liu, L. Zuo, X. Zhang, T. Ye, J. Chen, C.-Z. Li, G. Wu and H. Chen, *J. Mater. Chem. A*, 2016, **4**, 9430–9436.

33 F. Ye, J. Ma, C. Chen, H. Wang, Y. Xu, S. Zhang, T. Wang, C. Tao and G. Fang, *Adv. Mater.*, 2021, **33**, 2007126.

34 H. Min, M. Kim, S.-U. Lee, H. Kim, G. Kim, K. Choi, J. H. Lee and S. I. Seok, *Science*, 2019, **366**, 749–753.

35 F. Xie, C.-C. Chen, Y. Wu, X. Li, M. Cai, X. Liu, X. Yang and L. Han, *Energy Environ. Sci.*, 2017, **10**, 1942–1949.

36 J. Hu, L. Yang and J. Zhang, *Sol. RRL*, 2023, **7**, 2300187.

37 T. Du, T. J. Macdonald, R. X. Yang, M. Li, Z. Jiang, L. Mohan, W. Xu, Z. Su, X. Gao, R. Whiteley, C.-T. Lin, G. Min, S. A. Haque, J. R. Durrant, K. A. Persson, M. A. McLachlan and J. Briscoe, *Adv. Mater.*, 2022, **34**, 2107850.

38 T. Du, S. R. Ratnasingham, F. U. Kosasih, T. J. Macdonald, L. Mohan, A. Augurio, H. Ahli, C.-T. Lin, S. Xu, W. Xu, R. Binions, C. Ducati, J. R. Durrant, J. Briscoe and M. A. McLachlan, *Adv. Energy Mater.*, 2021, **11**, 2101420.

39 M. Anaya, J. F. Galisteo-López, M. E. Calvo, J. P. Espinós and H. Míguez, *J. Phys. Chem. Lett.*, 2018, **9**, 3891–3896.

40 R. Brenes, C. Eames, V. Bulović, M. S. Islam and S. D. Stranks, *Adv. Mater.*, 2018, **30**, 1706208.

41 R. Brenes, D. Guo, A. Osherov, N. K. Noel, C. Eames, E. M. Hutter, S. K. Pathak, F. Niroui, R. H. Friend, M. S. Islam, H. J. Snaith, V. Bulović, T. J. Savenije and S. D. Stranks, *Joule*, 2017, **1**, 155–167.

42 H.-H. Fang, S. Adjokatse, H. Wei, J. Yang, G. R. Blake, J. Huang, J. Even and M. A. Loi, *Sci. Adv.*, 2016, **2**, e1600534.

43 J. He, W.-H. Fang, R. Long and O. V. Prezhdo, *J. Am. Chem. Soc.*, 2019, **141**, 5798–5807.

44 S.-C. Liu, Z. Li, Y. Yang, X. Wang, Y.-X. Chen, D.-J. Xue and J.-S. Hu, *J. Am. Chem. Soc.*, 2019, **141**, 18075–18082.

45 Y. Tian, M. Peter, E. Unger, M. Abdellah, K. Zheng, T. Pullerits, A. Yartsev, V. Sundström and I. G. Scheblykin, *Phys. Chem. Chem. Phys.*, 2015, **17**, 24978–24987.

46 H. Wei, Y. Fang, P. Mulligan, W. Chuirazzi, H.-H. Fang, C. Wang, B. R. Ecker, Y. Gao, M. A. Loi, L. Cao and J. Huang, *Nat. Photon.*, 2016, **10**, 333–339.

47 P. Myagmarsereejid, S. Suragtkhuu, Q. T. Trinh, T. Gould, N. T. Nguyen, M. Bat-Erdene, E. Campbell, M. T. Hoang, W.-H. Chiu, Q. Li, H. Wang, Y. L. Zhong and M. Batmunkh, *npj 2D Mater. Appl.*, 2024, **8**, 38.

48 N. Aristidou, I. Sanchez-Molina, T. Chotchuangchutchaval, M. Brown, L. Martinez, T. Rath and S. A. Haque, *Angew. Chem., Int. Ed.*, 2015, **54**, 8208–8212.

49 H. Meng, K. Mao, F. Cai, K. Zhang, S. Yuan, T. Li, F. Cao, Z. Su, Z. Zhu, X. Feng, W. Peng, J. Xu, Y. Gao, W. Chen, C. Xiao, X. Wu, M. D. McGehee and J. Xu, *Nat. Energy*, 2024, **9**, 536–547.

50 R. A. Saha, W.-H. Chiu, G. Degutis, P. Chen, M. Filez, E. Solano, N. Orlov, F. De Angelis, R. Ariza, C. Meneghini, C. Detavernier, S. S. Mali, M. T. Hoang, Y. Yang, E. C. Garnett, L. Wang, H. Wang, M. B. J. Roeffaers and J. A. Steele, *ACS Nano*, 2024, **18**, 16994–17006.

51 J. F. Moulder, W. F. Stickle, P. E. Sobol and K. D. Bomben, *Handbook of X-ray Photoelectron Spectroscopy: A Reference Book of Standard Spectra for Identification and Interpretation of XPS Data*, Physical Electronics Division, Perkin-Elmer Corporation, 1992.

52 G. Chen, Y. Qiu, H. Gao, Y. Zhao, J. Feng, L. Jiang and Y. Wu, *Adv. Funct. Mater.*, 2020, **30**, 1908894.

53 S. Macpherson, T. A. S. Doherty, A. J. Winchester, S. Kosar, D. N. Johnstone, Y.-H. Chiang, K. Galkowski, M. Anaya, K. Frohna, A. N. Iqbal, S. Nagane, B. Roose, Z. Andaji-Garmaroudi, K. W. P. Orr, J. E. Parker, P. A. Midgley, K. M. Dani and S. D. Stranks, *Nature*, 2022, **607**, 294–300.

54 T. J. Jacobsson, J.-P. Correa-Baena, E. Halvani Anaraki, B. Philippe, S. D. Stranks, M. E. F. Bouduban, W. Tress, K. Schenk, J. Teuscher, J.-E. Moser, H. Rensmo and A. Hagfeldt, *J. Am. Chem. Soc.*, 2016, **138**, 10331–10343.

55 E. von Hauff and D. Klotz, *J. Mater. Chem. C*, 2022, **10**, 742–761.

56 A. Guerrero, J. Bisquert and G. Garcia-Belmonte, *Chem. Rev.*, 2021, **121**, 14430–14484.

57 M. V. Khenkin, E. A. Katz, A. Abate, G. Bardizza, J. J. Berry, C. Brabec, F. Brunetti, V. Bulović, Q. Burlingame, A. Di Carlo, R. Cheacharoen, Y.-B. Cheng, A. Colsmann, S. Cros, K. Domanski, M. Dusza, C. J. Fell, S. R. Forrest, Y. Galagan, D. Di Girolamo, M. Grätzel, A. Hagfeldt, E. von Hauff, H. Hoppe, J. Kettle, H. Köbler, M. S. Leite, S. Liu, Y.-L. Loo, J. M. Luther, C.-Q. Ma, M. Madsen, M. Manceau, M. Matheron, M. McGehee, R. Meitzner, M. K. Nazeeruddin, A. F. Nogueira, Ç. Odabaşı, A. Osherov, N.-G. Park, M. O. Reese, F. De Rossi, M. Saliba, U. S. Schubert, H. J. Snaith, S. D. Stranks, W. Tress, P. A. Troshin, V. Turkovic, S. Veenstra, I. Visoly-Fisher, A. Walsh, T. Watson, H. Xie, R. Yıldırım, S. M. Zakeeruddin, K. Zhu and M. Lira-Cantu, *Nat. Energy*, 2020, **5**, 35–49.

58 G. Tumen-Ulzii, C. Qin, T. Matsushima, M. R. Leyden, U. Balijipalli, D. Klotz and C. Adachi, *Sol. RRL*, 2020, **4**, 2000305.

59 A. S. R. Bati, P. Myagmarsereejid, M. Fronzi, K. Fan, P. Liu, Y. L. Zhong, P. L. Burn, I. R. Gentle, P. E. Shaw and M. Batmunkh, *Small Struct.*, 2024, **5**, 2300334.

60 Y. Dong, F. M. Rombach, G. Min, H. J. Snaith, C.-T. Lin, S. A. Haque and T. J. Macdonald, *Mater. Sci. Eng., R*, 2025, **162**, 100875.

61 G. Kresse and J. Hafner, *Phys. Rev. B*, 1993, **47**, 558–561.

62 G. Kresse and J. Furthmüller, *Comput. Mater. Sci.*, 1996, **6**, 15–50.

63 Q. T. Trinh, B. K. Chethana and S. H. Mushrif, *J. Phys. Chem. C*, 2015, **119**, 17137–17145.

64 Q. T. Trinh, K. F. Tan, A. Borgna and M. Saeys, *J. Phys. Chem. C*, 2013, **117**, 1684–1691.

65 Q. T. Trinh, K. Bhola, P. N. Amaniampong, F. Jérôme and S. H. Mushrif, *J. Phys. Chem. C*, 2018, **122**, 22397–22406.

66 Q. T. Trinh, A. V. Nguyen, D. C. Huynh, T. H. Pham and S. H. Mushrif, *Catal. Sci. Technol.*, 2016, **6**, 5871–5883.

67 Q. T. Trinh, A. Banerjee, Y. Yang and S. H. Mushrif, *J. Phys. Chem. C*, 2017, **121**, 1099–1112.

68 A. Nandula, Q. T. Trinh, M. Saeys and A. N. Alexandrova, *Angew. Chem., Int. Ed.*, 2015, **54**, 5312–5316.